Drift wave based modelling of poloidal spin-up precursor and stepwise expansion of transport barriers

G.M. Staebler, R.E. Waltz
General Atomics, San Diego, California

J.E. Kinsey*, G. Bateman, A.H. Kritz, T. Onjun, A. Pankin
Lehigh University, Bethlehem, Pennsylvania

P. Zhu, W. Horton
Institute for Fusion Studies, The University of Texas at Austin, Austin, Texas

United States of America

Abstract. The rich phenomenology of internal transport barriers (ITBs) observed in tokamaks includes a poloidal spin-up precursor for balanced injection neutral beam heating and stepwise expansion of the barrier for unbalanced injection. Examples of numerical simulations of these phenomena are presented. Two drift wave based predictive transport models (GLF23 and multimode) are used. Both models include the suppression of ion temperature gradient modes as the $\boldsymbol{E} \times \boldsymbol{B}$ shear approaches the computed maximum linear growth rate. Modelling of discharges with ITBs from the DIII-D, JET and TFTR tokamaks are compared.

1. Introduction

The ion temperature gradient (ITG) [1] and trapped electron mode (TEM) [2] drift wave instabilities have long been known to be unstable in tokamak plasmas. Recent 3-D non-linear simulations of these modes [3] have demonstrated that they can produce the level of heat loss observed in experiments. These non-linear simulations still require too much computer time to be of practical use for comparisons with more than a few experimental measurements. The present state of the art is also limited in its ability to include electron temperature gradient (ETG) drift waves [4] in the non-linear ITG/TEM simulations since they exist at much shorter wavelengths than the ITG/TEM modes. Drift wave based models attempt to approximate the first principal theoretical calculations of stability and non-linear transport in a computationally tractable model which can be compared with a variety of experiments.

Here we report some of the recent success of drift wave based transport modelling of internal transport barriers (ITBs), i.e. in the region of the plasma where at least the ion thermal transport has been reduced to the neoclassical level. The term drift wave based is used in this article to mean a theoretical model which computes the linear growth rates of drift waves locally and then computes the transport due to these modes using quasi-linear theory and a model for the saturated fluctuation amplitude. The two specific models which fit this description are the multimode model (MMM95), which pioneered this methodology [5–7] using the Wieland–Nordman fluid model [8–10], and the GLF23 model [11], which adopted the same method but uses a gyro-Landau fluid [12] treatment of the drift waves, including Landau damping and other kinetic effects, rather than the fluid limit employed by the Weiland–Nordman model. Both models include the ITG mode and trapped electron modes, which are the dominant contributors to ion and electron thermal transport, particle transport and ion momentum transport when they are unstable. These models have been shown to predict the energy confinement quite well over a large database of L mode and H mode tokamak discharges [13].

New physics must be added in order to model discharges with ITBs. An ITB can be produced by the suppression of ITG modes by $\boldsymbol{E} \times \boldsymbol{B}$ velocity shear. The suppression of ITG mode turbulence by equilibrium $\boldsymbol{E} \times \boldsymbol{B}$ velocity shear has been demonstrated in 3-D non-linear numerical simulations [14]. The simulations were shown to approximately follow a simple 'quench rule'. The turbulence is quenched (completely suppressed) when the $\boldsymbol{E} \times \boldsymbol{B}$ shear rate $\gamma_{\boldsymbol{E}\times\boldsymbol{B}}$ exceeds the maximum linear ITG mode growth rate of the wavenumber spectrum γ_{ITG} computed

without $\boldsymbol{E} \times \boldsymbol{B}$ shear. The quench rule is not the same as the simple linear stability rule for toroidal modes [15]. Non-linear effects were found to shift the quench point either above or below the point where $\boldsymbol{E} \times \boldsymbol{B}$ shear causes linear stability in toroidal geometry. The non-linear decorrelation mechanism [16, 17] was also found not to play a role, since the modes were quenched for smaller values of the $\boldsymbol{E} \times \boldsymbol{B}$ velocity shear than would be required for the decorrelation mechanism to even begin to have an effect. The quench rule is implemented in the models by introducing a net growth rate

$$\gamma_{net} = \gamma_{ITG} - \alpha_{\boldsymbol{E}\times\boldsymbol{B}}\gamma_{\boldsymbol{E}\times\boldsymbol{B}}$$

which is set to zero when it is negative. The multiplier $\alpha_{\boldsymbol{E}\times\boldsymbol{B}}$ is a constant of order one. This mechanism has been shown to be consistent with enhanced confinement regimes in tokamaks ranging from H mode to VH mode to ITBs (for a review, see Ref. [18]). Using simple models incorporating the quench rule, much of the phenomenology of $\boldsymbol{E} \times \boldsymbol{B}$ shear suppression of transport has been explored, giving useful insight into experiments and leading to new methods of controlling transport (for a review, see Ref. [19]). In order to have a predictive transport model incorporating the quench rule, the maximum linear ITG mode growth rate must be computed. Only then can the dependence of the transport suppression threshold on the safety factor profile, the Shafranov shift and many other important factors be accurately modelled.

The drift wave based models use the linear growth rate of both ITGs and TEMs in the quench rule. This goes beyond established theory since the non-linear simulations [14] were done only for ITG modes with no trapped electrons. However, it is known from linear theory that trapped electron modes can be stabilized by $\boldsymbol{E} \times \boldsymbol{B}$ shear [20].

The two models are similar in their ITG and TEM sectors but differ widely in the other contributions to transport. The GLF23 model has ETG modes contributing to electron thermal transport only. These modes are not subject to the quench rule due to their large growth rates. The multimode model has a formula for kinetic ballooning modes which gives additional transport in all channels (both heat and particle) and is also not affected by $\boldsymbol{E} \times \boldsymbol{B}$ shear. Thus, the transport in the ITB region where ITG modes and TEMs are quenched has quite different physics in the two models. Both models are inadequate in one way or another in modelling the transport within the ITB as discussed below.

Three examples are given illustrating the ability of the models to predict the onset and development of ITBs in tokamaks. The first two have been published elsewhere but the third is new. The first example [21] is a multimode simulation of the evolution of an optimized shear discharge on the JET tokamak. In this case the temperatures, density, q profile, sources, sinks and neutrals were evolved with multimode, but the toroidal rotation was taken from the experimental data. The second case [22] is a GLF23 simulation of a DIII-D discharge. Here the toroidal rotation was evolved but not the density or q profile. The sources and sinks were taken from an ONETWO code analysis. The stepwise expansion of the transport barrier is shown to result from competition between the toroidal rotation and diamagnetic plus poloidal velocity contributions to the $\boldsymbol{E} \times \boldsymbol{B}$ velocity. The third case is a modified GLF23 simulation of a TFTR discharge. In this discharge a poloidal spin-up precursor to the ITB was observed [23]. This is reproduced by the model evolving the ion temperature and $\boldsymbol{E} \times \boldsymbol{B}$ velocity in a very high resolution computation with a special numerical method [24]. It is worth noting that drift wave based models pose difficult numerical challenges. The quasi-linear theory produces a flux of energy, particles and viscous stress. The transport coefficients (of diffusivity and convection velocity) can be defined in different ways from these fluxes, which are strongly non-linear functions of the profile gradients with cross-couplings (off-diagonal terms) of similar strengths to those of the diagonal terms. The multimode model example was run on the BALDUR transport code [25]. The two GLF23 examples were run on the XPTOR code[1]. All three cases used different methods for defining the transport coefficients from the fluxes.

2. Momentum transport

Before discussing the three cases, a new extension of the momentum balance equations which determine the $\boldsymbol{E}\times\boldsymbol{B}$ velocity will be presented. The neoclassical equations for momentum transport are usually given in terms of the toroidal φ and parallel $\|$ momentum balance equations [26] ($\langle\,\rangle$ = flux surface average),

[1] The XPTOR code was written by J.E. Kinsey and G.M. Staebler, making use of existing data handling packages written by R.E. Waltz, J. Konings and G. Batemen and a transport equation solver written by G. Hammett. The code uses the MPI parallel library and is run on a Linux Beowulf cluster built by J. Candy.

$$\frac{\partial}{\partial t}(m_i n_i u_\varphi) + \left\langle (\boldsymbol{\nabla}\cdot\boldsymbol{\Pi}^A - \boldsymbol{S})\cdot\hat{\boldsymbol{e}}_\varphi \frac{R}{R_0}\right\rangle = 0 \qquad (1)$$

where

$$u_\varphi = \langle \boldsymbol{V}\cdot\hat{\boldsymbol{e}}_\varphi R\rangle / R_0 \qquad (2)$$

and

$$\frac{\partial}{\partial t}(m_i n_i u_\parallel) + \left\langle \left[(\boldsymbol{\nabla}\cdot(\boldsymbol{\Pi}^{neo}+\boldsymbol{\Pi}^A) - \boldsymbol{S}\right]\cdot\frac{\boldsymbol{B}}{B_0}\right\rangle = 0 \qquad (3)$$

where

$$u_\parallel = \langle \boldsymbol{V}\cdot\boldsymbol{B}\rangle / B_0. \qquad (4)$$

Here $\boldsymbol{\Pi}^{neo}$ is the neoclassical collisional contribution to the viscous stress, which vanishes in the toroidal direction φ, and $\boldsymbol{\Pi}^A$ is the viscous stress due to turbulence [20] plus the small classical collisional gyroviscosity. The external momentum source vector is $\boldsymbol{S}$. The magnetic field B_0 and major radius R_0 are evaluated at the magnetic axis. The inertia terms have been neglected since they are small. The neoclassical parallel viscous stress

$$\left\langle \boldsymbol{\nabla}\cdot\boldsymbol{\Pi}^{neo}\cdot\frac{\boldsymbol{B}}{B_0}\right\rangle = \mu^{neo}\left(u_\theta - K\frac{\partial T}{\partial\rho}\right) \qquad (5)$$

is usually assumed to be much larger than the contribution from turbulence [26]. The parallel momentum balance is also assumed to come to equilibrium faster than the other transport equations. With these orderings, the poloidal velocity

$$u_\theta = \rho B_0 \langle V_\theta / B_\theta\rangle / (R_0 q)$$

is determined by setting the neoclassical parallel viscous stress (Eq. (5)) to zero. This ordering has also been used in the first two examples in this article. The $\boldsymbol{E}\times\boldsymbol{B}$ velocity $u_{\boldsymbol{E}\times\boldsymbol{B}} = (c/B_0)(d\Phi/d\rho)$ is determined from radial force balance to be

$$u_{\boldsymbol{E}\times\boldsymbol{B}} + \frac{c}{eB_0 n_i}\frac{dp_i}{d\rho} = \left(c_2 u_\theta - \frac{\rho}{R_0 q}u_\varphi\right)\Big/ c_3 \qquad (6)$$

where

$$c_1 = \frac{\langle B^2\rangle}{B_0^2}, \quad c_2 = \frac{\langle RB_\varphi\rangle}{R_0 B_0}, \quad c_3 = \frac{\langle R^2\rangle}{R_0^2}. \qquad (7)$$

Using the neoclassical solution for the poloidal velocity, the $\boldsymbol{E}\times\boldsymbol{B}$ velocity is eliminated using Eq. (6) in terms of the three fields (u_φ, p_i, n_i) which are evolved by the transport equations. One problem with this approach is that the quasi-linear fluxes become functions of the second derivatives of the ion temperature and density through the $\boldsymbol{E}\times\boldsymbol{B}$ shear. This makes the transport equations third order in the gradients, introducing the need for unphysical boundary conditions [27]. If the ordering assumptions are relaxed so that the parallel momentum balance equation is on the same footing as the others, then an equation for the time evolution of the $\boldsymbol{E}\times\boldsymbol{B}$ velocity can be obtained [24]. The radial force balance equation (Eq. (6)) is used to eliminate the poloidal velocity in favour of the $\boldsymbol{E}\times\boldsymbol{B}$ velocity. The toroidal and parallel momentum balance equations are then combined to obtain an equation with only the toroidal and $\boldsymbol{E}\times\boldsymbol{B}$ velocities using

$$\frac{\rho}{R_0 q}\frac{(c_1 u_\varphi - c_2 u_\parallel)}{(c_2^2 - c_1 c_3)} = u_{\boldsymbol{E}\times\boldsymbol{B}} + \frac{c}{eB_0 n_i}\frac{dp_i}{d\rho}. \qquad (8)$$

The resulting equation is

$$\frac{\partial}{\partial t}\left[m_i n_i\left(u_{\boldsymbol{E}\times\boldsymbol{B}} + \frac{c}{eB_0 n_i}\frac{dp_i}{d\rho}\right)\right] + \left\langle\left[\boldsymbol{\nabla}\cdot(\boldsymbol{\Pi}^A + \boldsymbol{\Pi}^{neo}) - \bar{\boldsymbol{S}}\right]\cdot\hat{\boldsymbol{e}}_{\boldsymbol{E}\times\boldsymbol{B}}\right\rangle = 0 \qquad (9)$$

where

$$\hat{\boldsymbol{e}}_{\boldsymbol{E}\times\boldsymbol{B}} = \frac{\rho}{R_0 q}\left(c_1\frac{RB_\varphi}{R_0 B_0}\hat{\boldsymbol{e}}_\varphi - c_2\frac{\boldsymbol{B}}{B_0}\right)\Big/(c_2^2 - c_1 c_3). \qquad (10)$$

Using Eq. (9) keeps all of the turbulent fluxes (and viscous stresses) first order in the derivative of the time dependent fields (n_i, p_e, p_i, u_φ, $u_{\boldsymbol{E}\times\boldsymbol{B}}$). This equation was used only in the third example in this article. It is required to model the strong deviation from neoclassical poloidal flow observed in the poloidal spin-up precursor.

3. Multimode model simulations

The multimode transport model is used in the BALDUR time dependent predictive transport modelling code to simulate the onset and time evolution of ITBs in high performance JET and DIII-D discharges [21]. These transport simulations compute radial profiles as a function of time for the electron and ion temperatures, hydrogenic and impurity ion densities, magnetic q value, sources and sinks of heat and particles, and neutral particle densities. Boundary conditions are taken from experimental data just inside the separatrix or at the top of the H mode pedestal, when that pedestal forms. The toroidal velocity profile as a function of time is taken from experimental measurements, while the poloidal velocity profile is computed from neoclassical theory [28].

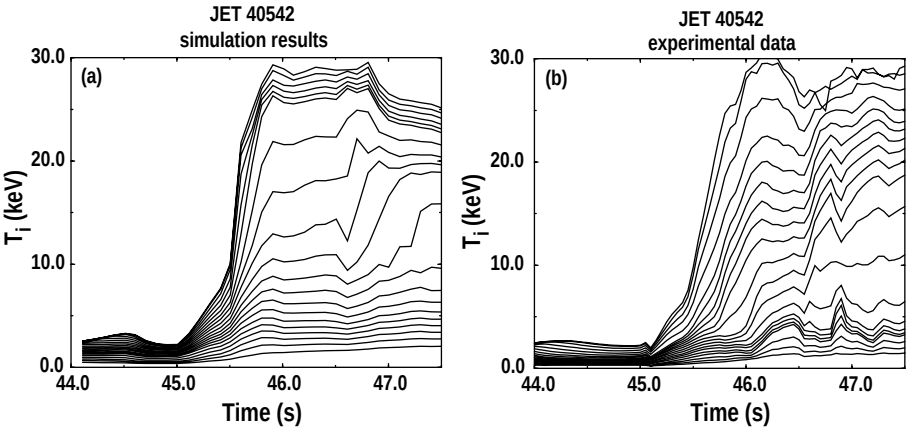

Figure 1. Ion temperature as function of time at equally spaced intervals in normalized minor radius in (a) simulations and (b) experiment for JET discharge 40542 with major radius 2.9 m, minor radius 0.94 m, toroidal field 3.6 T, plasma current 3.3 MA, line averaged density 2.5×10^{19} m^3 and 17 MW NBI heating. From Ref. [21].

The JET discharges are particularly complex: the BALDUR simulations follow the transition from ohmic to L mode, to the formation of an ITB, to the transition to H mode (implemented as a time dependent boundary condition in our simulations) and then to the subsequent motion of the ITB. The plasma current is ramped up while radiofrequency and neutral beam injection pre-heating is used to produce a broad current profile with low magnetic shear over a broad central region of the plasma.

The time evolution of the ion temperature profile for JET discharge 40542 is shown in Fig. 1, with results from the simulation results shown in Fig. 1(a) and the corresponding experimental measurements shown in Fig. 1(b). The curves in this figure show the ion temperature at equally spaced intervals in normalized minor radius as a function of time. The top curve in this figure represents the peak temperature as a function of time, which is generally at or near the magnetic axis, while the bottom curve represents the lowest temperature, which is generally at the edge of the plasma. ITBs are characterized by a wider spacing between adjacent curves (steeper gradients). It can be seen in Fig. 1 that an ITB forms near the magnetic axis (close to the top curve) between 45.8 and 46.5 s in both the simulation (a) and the experiment (b). The transport barrier then moves closer to the edge of the plasma (lower curves) between 46.5 and 46.9 s in both simulation and experiment. Similar behaviour is observed in simulations of other high performance discharges in JET and DIII-D [28].

The simulation shown here uses a recent version of the multimode model with $\boldsymbol{E} \times \boldsymbol{B}$ flow shear stabilization using the quench rule in the Weiland model for drift modes that includes finite beta and low magnetic shear effects, as well as the Bateman–Scott model for drift Alfvén modes near the plasma edge [7]. Similar results are obtained using the Hamaguchi–Horton stabilization model that includes the effects of low magnetic shear and high flow shear [29]. In this Hamaguchi–Horton model, the quasi-linear transport coefficients are divided by $1 + (\gamma_s/\gamma_{sc})^2$, where $\gamma_{sc} \approx 1$ and

$$\gamma_s = \sqrt{\frac{m_i}{T_e}} \left| \frac{R \partial_\psi (E_r/RB_\theta)}{\partial_\psi \ln q} \right|. \tag{11}$$

This model enhances the $\boldsymbol{E} \times \boldsymbol{B}$ shear suppression in regions of weak magnetic shear. Note that the turbulence is reduced but not quenched in the Hamaguchi–Horton model. In this simulation, each of the three contributions to the $\boldsymbol{E} \times \boldsymbol{B}$ velocity (Eq. (6)) have comparable magnitudes during the formation and motion of the ITB. The flow shear in the poloidal velocity (U_θ) contribution has a sharp positive peak at the inner edge of the transport barrier and a negative peak at the outer edge (as a function of minor radius). The peak value of flow shear in the toroidal velocity ($U\varphi$) contribution (taken from experimental measurements in this simulation) remains at the outer edge of the ITB as the barrier shifts outwards in minor radius between 46.0 and 47.5 s. The timing and location of the ITB transition is sensitive to the multiplier $\alpha_{\boldsymbol{E}\times\boldsymbol{B}}$ in the quench rule.

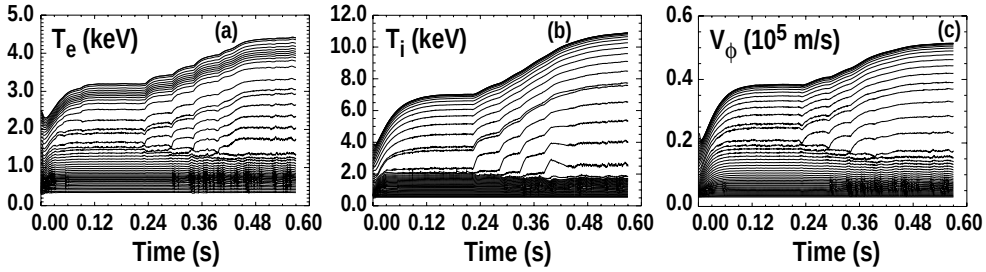

Figure 2. Time evolution of (a) electron temperature, (b) ion temperature and (c) toroidal velocity predicted by the GLF23 model for DIII-D NCS discharge 87436. Values are shown at various radii with a spacing of $\Delta\rho = 0.02$. From Ref. [22].

This multiplier is known to vary with magnetic shear and elongation from the non-linear simulations but is taken to be a constant in the models. It has not been possible to obtain a good fit to a variety of discharges with a single value of $\alpha_{\boldsymbol{E}\times\boldsymbol{B}}$. More non-linear simulations are needed to develop a model for the parametric dependences in $\alpha_{\boldsymbol{E}\times\boldsymbol{B}}$. The ITB threshold is a critical test of the $\boldsymbol{E}\times\boldsymbol{B}$ shear suppression model and its dependence on local plasma conditions.

4. GLF23 simulation of stepwise barrier expansion

The GLF23 transport model has been used to dynamically follow $\boldsymbol{E}\times\boldsymbol{B}$ shear driven bifurcations in the energy and toroidal momentum confinement in DIII-D discharges with an ITB [22]. Taking the density profiles, equilibrium, sources and sinks from an ONETWO analysis, the simulations are initialized with temperature and toroidal velocity profiles scaled down from the experimental profiles (at a given diagnostic time) to pre-barrier levels, and the temperature and toroidal velocity profiles are evolved while self-consistently computing the effects of $\boldsymbol{E}\times\boldsymbol{B}$ shear stabilization using the model predicted profiles. The ITB is predicted to form and expand in a stepwise fashion, with the core temperatures and toroidal rotation displaying an abrupt series of jumps during the barrier formation and expansion. These results are consistent with experimental observations. The toroidal classical gyroviscosity is too small to be consistent with the observed toroidal rotation profile in the region where the ITG modes are quenched by $\boldsymbol{E}\times\boldsymbol{B}$ velocity shear. The gyroviscosity was enhanced to the level of the neoclassical ion thermal diffusivity in these simulations. The cause of this anomalous momentum transport within the ITB is not explained by the GLF23 model or any existing theory.

In Fig. 2, the dynamic formation of an ITB resulting from an $\boldsymbol{E}\times\boldsymbol{B}$ shear driven bifurcation is demonstrated for a DIII-D negative central shear (NCS) discharge with an L mode edge. Shown are the ion temperature and toroidal velocity predicted by the GLF23 model versus time. In the simulations, the step transitions are a direct result of local $\boldsymbol{E}\times\boldsymbol{B}$ driven transport bifurcations. At each transition, dips in the electron temperatures and toroidal velocity are clearly evident as the $\boldsymbol{E}\times\boldsymbol{B}$ shear rate drops below the maximum linear growth rate at the leading edge of the barrier. As a result, $\boldsymbol{E}\times\boldsymbol{B}$ shear stabilization is transiently lost and the local thermal and toroidal momentum transport increases dramatically. The stiffness of the model then results in rapid propagation of the perturbation across the plasma core. Here, the dips are due to competition between the toroidal and diamagnetic plus poloidal velocity terms within the $\boldsymbol{E}\times\boldsymbol{B}$ shear rate, which frustrates the otherwise continuous expansion of the ITB. The shear in the diamagnetic plus poloidal terms has the opposite sign from the toroidal rotation shear at the leading edge of the barrier. Since the toroidal rotation term dominates, a local increase in the ion temperature gradient reduces the net $\boldsymbol{E}\times\boldsymbol{B}$ shear at the front of the barrier, which can cause a transient loss of $\boldsymbol{E}\times\boldsymbol{B}$ shear suppression. A smooth ITB expansion is predicted for counter-NBI since the sign of the toroidal rotation shear is now the same as the diamagnetic plus poloidal velocity shear. Steps have not been observed in counter-injected DIII-D discharges with ITBs. The barrier expansion phase begins deep in the core region where the drift wave transport is stabilized by negative magnetic shear, high T_i/T_e and fast ion dilution, and the toroidal rotation dominates

the $\boldsymbol{E} \times \boldsymbol{B}$ shear. The ITB expands through a series of step transitions until the positive magnetic shear region is reached and the $\boldsymbol{E} \times \boldsymbol{B}$ velocity shear can no longer exceed the rising ITG growth rate.

Overall, we find that both the height and the timing of the steps accompanying the expansion of the leading edge of the barrier are sensitive to the proximity to the $\boldsymbol{E} \times \boldsymbol{B}$ shear driven ITB threshold and the rate at which it is approached. The ITB threshold is determined by the plasma conditions including, for example, density and temperature gradients, auxiliary heating power and toroidal momentum input. Time variations in the densities, q profile, sources and sinks all have an impact on the character, timing and number of steps (if present) by changing the growth rate and $\boldsymbol{E} \times \boldsymbol{B}$ shear profile. Here, those quantities were held fixed in time and therefore we do not attempt a quantitative comparison of the timing of the steps with experimental data. There are other mechanisms which could cause stepwise expansions in the experiments, such as MHD instabilities slowing the expansion across low order rational safety factor surfaces. The modelling shows that the drift wave physics can also produce stepwise expansion dynamics.

5. Simulation of a poloidal spin-up precursor

The third example is a simulation of a TFTR discharge [23]. This discharge had reversed magnetic shear near the centre and made a transition to enhanced confinement after the neutral beam power was increased. The neutral beam power was balanced for no net toroidal torque. Before the strong rise in stored energy indicating the formation of an ITB, a remarkably large poloidal velocity was observed to develop in a very narrow layer, as shown in Fig. 3(a). This is the poloidal velocity of carbon but the velocity is so large compared with the diamagnetic velocity that it is by far the dominant contribution to the $\boldsymbol{E} \times \boldsymbol{B}$ velocity. This poloidal spin-up precursor grows up to its peak within the 20 ms integration time of the measurement. It then decays away over some 100 ms.

In previous work, an analytic model has been used to show that this monopolar velocity excursion can be fitted by a solution to the momentum balance equations (Eqs (2) and (5)) called a jet solution [30]. The poloidal flow is generated by an instability of the equations. When the $\boldsymbol{E} \times \boldsymbol{B}$ velocity shear is in the

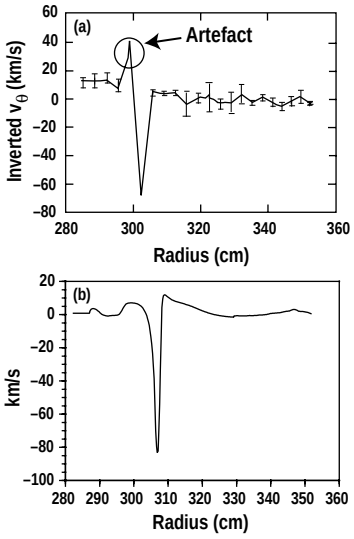

Figure 3. (a) Poloidal velocity of ^{6}C ions measured for TFTR discharge 104981 at 1.81 s (Fig. 2 of Ref. [23]). (b) The $\boldsymbol{E} \times \boldsymbol{B}$ velocity computed with GLF23 at 1.824 s modelling time for the same TFTR discharge.

range where the magnitude of the turbulent viscous stress is dropping with increasing velocity shear, due to the reduction of the drift wave turbulence, the incremental viscosity (minus the derivative of the viscous stress with respect to the $\boldsymbol{E} \times \boldsymbol{B}$ velocity shear) is negative. A negative incremental viscosity produces an instability in the poloidal velocity with a growth rate that increases with the wavenumber of the perturbation squared [24]. Owing to the presence of the neoclassical viscous damping of the poloidal velocity, this instability saturates at a wavenumber determined by the ratio of the neoclassical collisional damping rate to the incremental viscosity due to turbulence. A narrow monopolar $\boldsymbol{E} \times \boldsymbol{B}$ velocity excursion from its neoclassical value is the quasi-steady state on the collisional damping rate timescale. This steady state jet solution was shown to be a type of topological soliton [30]. The integral of the velocity excursion is topologically conserved.

A numerical solution of a modified version of GLF23 has now been obtained for the same TFTR discharge at 1.824 s, as shown in Fig. 3(b). Only the ion temperature and $\boldsymbol{E} \times \boldsymbol{B}$ velocity were evolved. The electron temperature profile was taken from the experiment. It does not participate directly in the determination of the $\boldsymbol{E} \times \boldsymbol{B}$ velocity. The sources and densities, electron temperature, toroidal velocity, magnetic geometry etc. were interpolated in time from a TRANSP analysis of TFTR discharge 104981. The simulation was run from 1.79 to 1.85 s. A

more complete discussion of the simulation shown in Fig. 3(b) and the special numerical scheme used will be reported in Ref. [24]. The toroidal velocity from the experiment was used but it does not contribute to the narrow jet. A very fine grid was used (300 grid points over the full radius). The time step was 0.12 ms, which is shorter than the poloidal damping time (3.9 ms) at the radius of the jet. The $\boldsymbol{E} \times \boldsymbol{B}$ velocity jet grew spontaneously in a few milliseconds close to the same location as that observed in the experiment. The growth rate begins to increase rapidly with radius at this location. The jet solution persists for about 40 ms before decaying as the experimental profiles evolve. The ion temperature shows some steepening at the location of the jet. However, since the ion neoclassical thermal diffusion is much larger than the collisional gyroviscosity [31], the change in the $\boldsymbol{E} \times \boldsymbol{B}$ velocity gradient is much larger than the change in the temperature gradient. The analytic model [30] showed that the jet solution shrinks and then disappears as the diamagnetic velocity gradient increases. Once the diamagnetic velocity gradient is large enough to quench the turbulence no jet can exist.

The numerical simulation shows that the jet is somewhat fluctuating with finer scale features appearing and then disappearing. These finer scale fluctuations are partially suppressed in the numerical scheme for numerical stability so the jet shown in Fig. 3(b), which spans about 12 grid points, is in effect averaged over the grid scale and the time step. The measurement of the poloidal spin-up precursor was primarily on just one channel and was averaged over 20 ms. The spatial resolution is 3 cm [23]. It may be that the poloidal velocity is not steady but is bursty on timescales finer than the 20 ms integration time. The numerical simulation tends to have this property with the bursts appearing in the same localized region.

The agreement between the simulation and the experiment in this case is only achieved by adjusting the GLF23 model parameters. This departs from the philosophy of the model since it has been constructed by fitting (growth rates and the saturated fluctuations level) to theoretical calculations without adjustments from experimental data [11]. In order to obtain a good fit to the ion temperature profile the fast ion and impurity dilution had to be eliminated. The trapped electron mode was giving a large ion energy pinch due to the hollow thermal ion density. The multiplier ($\alpha_{\boldsymbol{E}\times\boldsymbol{B}}$) on the $\boldsymbol{E} \times \boldsymbol{B}$ shear also had to be turned down significantly. The ion temperature profile was well fitted with no $\boldsymbol{E} \times \boldsymbol{B}$ shear term. The Shafranov shift was sufficient to improve ion transport. This is consistent with the fact that the experimental discharge has not yet made the transition to enhanced confinement at this time. The $\boldsymbol{E} \times \boldsymbol{B}$ shear was multiplied by 0.01 in the simulation of Fig. 3(b). A larger value produces a smaller amplitude jet and a value near one produces a transport barrier at a larger radius without a jet. The computed growth rate in the region of the jet was about 0.03 Cs/a (Cs=$\sqrt{T_e/m_i}$). This would have to be increased to 3.0 Cs/a in order to reconcile the jet solution with the standard quench rule. Such a large growth rate is not likely for ITG or TEM modes. Another possibility is that the predominantly TEM turbulence in this region does not follow the quench rule. Rather, it could be suppressed, but not totally turned off, by $\boldsymbol{E} \times \boldsymbol{B}$ shear. A power law suppression factor [16, 17, 29] would allow the $\boldsymbol{E} \times \boldsymbol{B}$ velocity shear to greatly exceed the linear growth rate without completely reducing the transport to neoclassical. A third possibility is that ETG modes produce some ion momentum transport which is not included in the model. This would allow the momentum diffusivity to decrease as the $\boldsymbol{E} \times \boldsymbol{B}$ velocity shear increases well beyond the local ITG mode growth rate to the much larger ETG mode growth rate at short wavelengths. These are open questions related to the well known inconsistencies between the quench rule and experiment [19]. For example, quasi-linear theory predicts that ion momentum and electron particle transport should become neoclassical if the ITG modes and TEMs are quenched by $\boldsymbol{E} \times \boldsymbol{B}$ shear. Experimentally, particle and ion toroidal momentum transport are often not reduced to neoclassical values within transport barrier regions with neoclassical ion thermal transport.

6. Summary

Drift wave based transport models (multimode, GLF23) have been used to simulate the evolution of ITBs in a number of discharges from several tokamaks. Three examples have been given in this article. The models reproduce the onset and expansion of the ITBs fairly accurately. The success of these models is a confirmation of the ITG mode physics. In the models, ITG modes dominate the ion thermal and momentum transport prior to the formation of an ITB where $\boldsymbol{E} \times \boldsymbol{B}$ velocity shear quenches the ITG mode. The exact timing of the barrier

formation and the threshold power or torque required are sensitive to the local plasma parameters. Attempts to simulate a discharge close to a transport barrier threshold can fail badly because the simulation ends up on the wrong side of the threshold. This makes it difficult to assess the statistical accuracy of the models for discharges with transport barriers. On the other hand, this same sensitivity makes the threshold a strong test of the theory of ITG suppression by $\boldsymbol{E} \times \boldsymbol{B}$ shear. The modelling of experimental discharges shows that the quench rule works well for many cases but the data cannot rule out a power law suppression model. In the case of the poloidal spin-up precursor the standard quench rule does not appear to work. The quench rule for ITG modes may still be operative but the impact of $\boldsymbol{E} \times \boldsymbol{B}$ velocity shear on the remaining instabilities is an open theoretical question. There are still many unresolved issues concerning tokamak transport. The ITBs provide a laboratory where non-ITG transport mechanisms can be studied. The transport due to ETG modes in the GLF23 model has not been guided by nonlinear turbulence simulations and thus has a lower level of confidence than that of the ITG modelling. Non-linear simulations of the effect of $\boldsymbol{E} \times \boldsymbol{B}$ shear on trapped electron mode turbulence are needed to provide a stronger theoretical basis for the application of the quench rule to these modes. The kinetic ballooning model in multimode is primitive. These modes could be included in the linear growth rate calculations by improving the electromagnetic parts of the models and extending the magnetic geometry to shaped equilibria. The current state of drift wave based modelling of ITBs is represented by the three examples given in this article. The models are capable of reproducing interesting dynamical phenomena such as stepwise barrier expansion and the poloidal spin-up precursors. These milestones indicate that the drift wave theory of tokamak transport is on the right track.

Acknowledgements

We thank R.E. Bell for making the TFTR data available to us. This work has been supported by the US Department of Energy under Grants DE-FG02-92ER54141 and DE-FG03-95ER54309.

References

[1] Coppi, B., Rosenbluth, M.N., Sagdeev, R.Z., Phys. Fluids **10** (1966) 582.
[2] Kadomtsev, B.B., Pogutse, O.P., Sov. Phys.–Dokl. **14** (1969) 470.
[3] Beer, M.A., et al., Phys. Plasmas **4** (1997) 1792.
[4] Rozhanski, V.A., JETP Lett. **34** (1981) 56.
[5] Bateman, G., Kinsey, J.E., Kritz, A.H., Redd, A.J., Weiland, J., in Fusion Energy 1996 (Proc. 16th Eur. Conf. Montreal, 1996), Vol. 2, IAEA, Vienna (1996) 559.
[6] Bateman, J.E., Kritz, G., Kinsey, A.H., Redd, A.J., Weiland, J., Phys. Plasmas **5** (1998) 1793.
[7] Bateman, G., et al., in Fusion Energy 1998 (Proc. 17th Int. Conf. Yokahama, 1998), Vol. 4, IAEA, Vienna (1998) 1569.
[8] Nordman, H., Weiland, J., Jarmen, A., Nucl. Fusion **30** (1990) 983.
[9] Weiland, J., Hirose, A., Nucl. Fusion **32** (1992) 151.
[10] Nilsson, J., Weiland, J., Nucl. Fusion **34** (1994) 803.
[11] Waltz, R.E., et al., Phys. Plasmas **4** (1997) 2482.
[12] Hammett, G., Perkins, F., Phys. Rev. Lett. **64** (1990) 3019.
[13] Boucher, D., et al., Nucl. Fusion **40** (2000) 1955.
[14] Waltz, R.E., Kerbel, G.D., Milovich, J., Hammett, G.W., Phys. Plasmas **2** (1995) 2408.
[15] Waltz, R.E., Dewar, R.L., Garbet, X., Phys. Plasmas **5** (1998) 1784.
[16] Shaing, K.C., Lee, G.S., Carreras, B.A., Houlberg, W.A., Crume, E.C., Jr., in Plasma Physics and Controlled Nuclear Fusion Research 1988 (Proc. 12th Int. Conf. Nice, 1988), Vol. 2, IAEA, Vienna (1989) 13.
[17] Biglari, H., Diamond, P.H., Terry, P.W., Phys. Fluids B **2** (1990) 1.
[18] Burrell, K.H., Phys. Plasmas **4** (1997) 1499.
[19] Staebler, G.M., Plasma Phys. Control. Fusion **40** (1997) 569.
[20] Dominguez, R.R., Staebler, G.M., Phys. Fluids B **5** (1993) 3876.
[21] Zhu, P., Bateman, G., Kritz, A., Horton, W., Phys. Plasmas **7** (2000) 2898.
[22] Kinsey, J.E., Staebler, G.M., Burrell, K.H., Austin, M.E., Waltz, R.E., Phys. Rev. Lett. **86** (2001) 814.
[23] Bell, R.E., Levinton, F.M., Batha, S.H., Synakowski, E.J., Zarnstorff, M.C., Phys. Rev. Lett. **81** (1998) 1429.
[24] Staebler, G.M., Kinsey, J.E., Consequences of Momentum Transport due to Driftwave Turbulence (in preparation).
[25] Singer, C.E., et al., Comput. Phys. Commun. **49** (1988) 275.

[26] Hinton, F.L., Kim, Y.-B., Nucl. Fusion **34** (1994) 899.
[27] Taylor, J.B., Connor, J.W., Helander, P., Phys. Plasmas **5** (1998) 3065.
[28] Zhu, P., Horton, W., Sugama, H., Phys. Plasmas **6** (1999) 2503.
[29] Hamaguchi, S., Horton, W., Phys. Fluids B **4** (1992) 319.
[30] Staebler, G.M., Phys. Rev. Lett. **84** (2000) 3610.
[31] Tsang, K.T., Frieman, E.A., Phys. Fluids **19** (1976) 747.

(Manuscript received 8 October 2000
Final manuscript accepted 12 March 2001)

E-mail address of G.M. Staebler:
Gary.Staebler@gat.com

Subject classification: F2, Tt; D0, Tt